Journal of Solid State Electrochemistry (2022) 26:2501–2514
https://doi.org/10.1007/s10008-022-05246-3

ORIGINAL PAPER

Is there a common reaction pathway for chromium sulfides as anodes in sodium-ion batteries? A case study about sodium storage properties of MCr_2S_4 (M = Cr, Ti, Fe)

Felix Hartmann[1] · Lina Liers[1] · Martin Etter[2] · Huayna Terraschke[1] · Wolfgang Bensch[1]

Received: 31 May 2022 / Revised: 14 July 2022 / Accepted: 16 July 2022 / Published online: 15 August 2022

Abstract
We present new insights into the electrochemical properties of three metal sulfides MCr_2S_4 (M = Cr, Ti, Fe) probed as anode materials in sodium-ion batteries for the first time. The electrodes deliver decent reversible capacities and good long-term cycle stability, e.g., 470, 375, and 524 mAh g^{-1} are obtained after 200 cycles applying 0.5 A g^{-1} for M = Cr, Ti, and Fe, respectively. The reaction mechanisms are investigated via synchrotron-based X-ray powder diffraction and pair distribution function analyses. The highly crystalline educts are decomposed into Na_2S nanoparticles and ultra-small metal particles during initial discharge without formation of intermediate $NaCrS_2$ domains as previously reported for $CuCrS_2$ and $NiCr_2S_4$. After a full cycle, the structural integrity of MCr_2S_4 (M = Cr, Ti, Fe) is not recovered. Thus, the Na storage properties are attributed to redox reactions between nanoscopic to X-ray amorphous conversion products with only local atomic correlations M···S/S···S in the charged and M···M/Na···S in the discharged state.

Keywords Anode materials · Chromium sulfides · High-energy X-ray diffraction · Pair distribution function · Reaction mechanism · Sodium-ion batteries

Introduction

An uneven and geopolitically problematic Li world distribution as well as today's indispensability of rechargeable lithium-ion batteries (LIBs) in mobile electronics, e.g., smartphones and electric vehicles, causes the continuous rise in Li demand and call for alternative electrical energy storages [1–4]. One widely studied promising candidate is the sodium-ion battery (SIB), because Na is very cheap, highly abundant, and easily accessible, supporting a green and economic chemistry for battery production [5–10]. Although the electrochemical properties of Na^+/Na are similar to Li^+/Li, the greatest challenge for SIBs is the identification of an appropriate anodic electrode material, because untreated graphite as utilized in LIBs is unsuitable for SIBs [10–13]. Conversion-type electrodes promise high energy densities [14, 15], because the components are commonly reduced to their elemental state via formation of alkali metal salts such as Na_3P [16, 17], NaCl [18, 19], or Na_2Ch (e.g., Ch = O, S, Se) [20–26]. Several transition metal sulfides (TMSs) have been identified as promising anode materials for SIBs and exhibit good electrochemical properties if cycled vs. Na^+/Na, such as high cycle life, good rate capability and superior energy densities [27]. Prominent examples are, e.g., FeS_2 [28–31], Fe_3S_4 [32–34], $CuFeS_2$ [35], CoS [36–38], NiS [39–41], $NiCo_2S_4$ [42–45], or VS_2 [46]. Few investigations addressed the application of Cr sulfide electrodes in SIBs, i.e., $NaCrS_2$ [47] and $NaCr_{2/3}Ti_{1/3}S_2$ [48] as cathodes or $CrPS_4$ [49] and $CuCrP_2S_6$ [50], $CuCrS_2$ [21], and $NiCr_2S_4$ [22] as anodes. The two latter exhibit pseudo-layered structures composed of $[CrS_2]^{x-}$ slabs alternating with layers containing tetrahedrally coordinated Cu^+ or octahedrally coordinated Ni^{2+} cations, respectively [51, 52]. These arrangements provide Na storage via reversible sodium insertion–transition metal extrusion by generation of crystalline $NaCrS_2$-like intermediates similar to

✉ Felix Hartmann
fhartmann@ac.uni-kiel.de

✉ Wolfgang Bensch
wbensch@ac.uni-kiel.de

[1] Institute of Inorganic Chemistry, Christian-Albrecht University of Kiel, Max-Eyth-Str. 2, 24118 Kiel, Germany

[2] Deutsches Elektronen-Synchrotron (DESY), Notkestr. 85, 22607 Hamburg, Germany

lithium insertion–copper extrusion reactions earlier found for $Cu_{2.33}V_4O_{11}$ [53], $CuTi_2S_4$ [54], $CuCrS_4$ [54], or $CuCr_2Se_4$ [55]. Such charge storage mechanisms show similarity to intercalation/deintercalation reactions widely utilized in commercial LIBs [2, 56–59] because discharge/charge processes require only small volume changes compared to full conversion. Hence, the contacts between the reaction products and the current collectors remain well-preserved yielding higher cycle life. The transition metal extrusion additionally boosts the electrodes cycle life by generation of nanosized, electrically conducting metals such as Cu or Ni [21, 22]. These investigations prompted us to take a closer look at comparable Cr sulfides.

Compounds with the general composition MCr_2S_4 (M = 3d transition metals) crystallize either in the Cr_3S_4 structure type (Fig. 1a, space group (SG) $I12/m1$, no. 12) (M = Ti, V, Cr, and Ni) or in the spinel structure type (Fig. 1b, SG $Fd\bar{3}m$, no. 227) (M = Mn, Fe, Co, Cu, and Zn) [60, 61]. The Cr_3S_4 structure type can be described as an ordered defect variant intermediate between the NiAs and CdI_2 structure types: Edge-sharing CrS_6 octahedra form fully occupied layers with the stoichiometry CrS_2 and 50% of octahedral sites between these $[CrS_2]^{x-}$ slabs are occupied by M^{2+}, and 50% are empty [62]. Thus, compounds crystallizing in this structure type are regarded as layer-like materials (Fig. 1a). The precise structural description is, however, more complicated for each MCr_2S_4, because the cation distributions $M^{2+/3+}$:$Cr^{3+/2+}$ in fully and half occupied layers depend on the choice of M [52, 63, 64]. For example, Ti and Cr atoms share octahedral sites in fully occupied layers and remaining Cr atoms are located in the half occupied layers for $TiCr_2S_4$ as revealed by neutron scattering experiments [65]. The few investigations about accurate cation distributions in monoclinic $M_1M_2X_4$ (M = Ti, V, Cr, Ni; X = S, Se, Te) indicate that the site preference in fully occupied layers decreases in the order Ti > Cr ≈ V > Ni [52]. In contrast, the spinel structure is composed of S^{2-} anions arranged in a close-packed fcc lattice with M^{2+} cations occupying 1/8 of the tetrahedral and Cr^{3+} cations 1/2 of the octahedral voids (Fig. 1b) [66–69]. The thermodynamically favored arrangement of cations in MCr_2S_4 mainly depends on the octahedral site preference energy (OSPE) of $M^{2+/3+}$ [70]. Thus, high OSPEs (e.g., V^{2+} and Ni^{2+}) drive crystallization in the Cr_3S_4 structure type, whereas low OSPEs (e.g., Fe^{2+} and Zn^{2+}) prefer crystallization in the spinel structure [70].

We selected Cr_3S_4 (CS) and $TiCr_2S_4$ (TCS), both crystallizing in the Cr_3S_4-type, as well as cubic $FeCr_2S_4$ (FCS) for our investigations. High theoretical capacities Q(CS) = 754.3 mAh g^{-1}, Q(TCS) = 765.4 mAh g^{-1}, and Q(FCS) = 744.2 mAh g^{-1} are calculated for full conversion reaction of all cations to their elemental states according to the following:

$$MCr_2S_4 + 8\ Na^+ + 8\ e^- \rightarrow M^0 + 2\ Cr^0 + 4\ Na_2S \quad (1)$$

here, we present the first study about electrochemical performances of the title compounds as anode materials for SIBs analyzed by galvanostatic discharge–charge (GDC) cycling and cyclic voltammetry (CV). Moreover, new insights into charge storage properties during Na uptake and release of Cr sulfides in terms of a structural, mechanistic view are presented by results of synchrotron-based, high-energy X-ray powder diffraction (XRPD), and total scattering X-ray experiments to calculate pair distribution functions (PDFs).

Experimental

Synthesis of pristine materials

The pristine materials were synthesized by high-temperature solid-state reactions. Stoichiometric amounts of Cr (Alfa Aesar, 99%), Fe (Alfa Aesar, 99.9%), Ti (Chempur, 99.5%), and S (Chempur, 99.999%) corresponding to Cr_3S_4, $TiCr_2S_4$, and $FeCr_2S_4$ were each mixed and ground in mortars. The mixtures were placed in quartz tubes, which were sealed under vacuum ($< 10^{-4}$ mbar) and heated at 450 °C for 24 h and subsequently at 800 °C (FCS) or 1000 °C (CS, TCS) for 72 h in a furnace before cooling to room temperature. Each

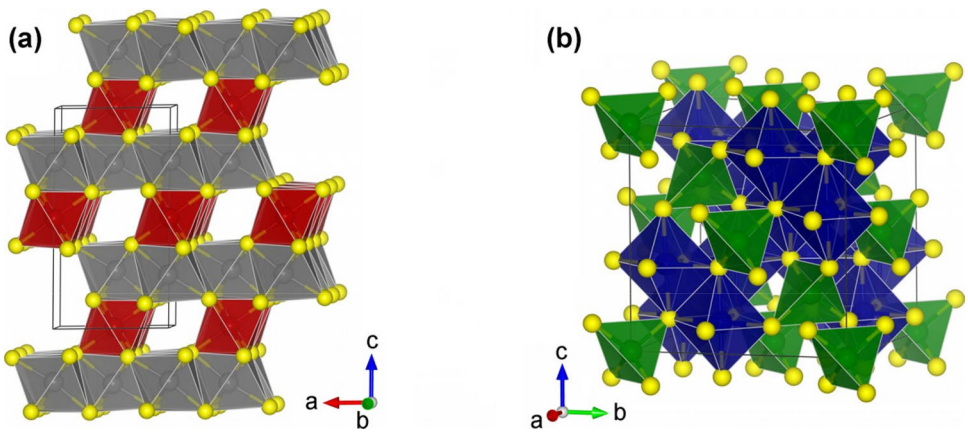

Fig. 1 Crystal structures of **a** monoclinic MCr_2S_4 with S (yellow atoms), Cr (in gray and/or red octahedra), M = Ti, V, Ni, Cr (in gray and/or red octahedra) and **b** cubic MCr_2S_4 with S (yellow atoms), Cr (in blue octahedra), M = Mn, Fe, Co, Cu, Zn (in green tetrahedra). Created with Vesta v3 [71]

product was crushed in a mortar, followed by characterization with XRPD. For CS and FCS, pellets were pressed and annealed at 800 °C (FCS) and 1000 °C (CS) for 168 h again, cooled to room temperature and crushed in mortars.

Electrochemical characterization

Film electrodes were prepared by suspending mixtures of 70 wt% MCr_2S_4, 20 wt% Super C65 carbon (Timcal), and 10 wt% polyvinylidene difluoride (PVDF) (Solvay) in *N*-methyl-2-pyrrolidone (Fisher Bioreagens, 99.8%) in a Retsch MM400 ball mill for 20 min at 15 Hz. The suspensions were spread on carbon coated Cu foil via doctor-blade casting method. Afterwards, they were dried for > 24 h at room temperature and at 60 °C in vacuum for about 12 h. For ex situ characterization, pellet electrodes were prepared by first mixing 70 wt% MCr_2S_4 and 30 wt% Super C65 (Timcal) in a Retsch MM400 ball mill for 30 min at 10 Hz and then pressing parts of these mixtures into pellets. Swagelok®-type test cells were assembled in an Ar-filled glovebox. In each cell, either a circular electrode disk ($d = 10$ mm, active material mass m(CS) = 1.5–2.1 mg cm^{-2}, m(TCS) = 1.4–1.5 mg cm^{-2}, and m(FCS) = 1.3–1.6 mg cm^{-2}) or pellet electrode ($d = 10$ mm, active material mass m(CS) = 12–25 mg cm^{-2}, m(TCS) = 17–24 mg cm^{-2}, and m(FCS) = 12–22 mg cm^{-2}) was covered by a Celgard® membrane and two glass fiber filter disks (Whatman) as separators, wetted by 1 m sodium trifluoromethanesulfonate $NaCF_3SO_3$ (Sigma-Aldrich, 98%) in bis(2-methoxyethyl)ether (diglyme, Acros, 99 + %, anhydrous) as electrolyte solution, and layered by a circular Na metal disk as the counter electrode. GDC measurements were performed on a Neware BTS 3000 and an MTI BST8-WA battery analyzer applying constant current constant voltage (CCCV) mode for performance tests (film electrodes). A current density of 0.1 A g^{-1} was always applied for the 1st cycle and the end current of the CCCV mode. For ex situ characterization (pellet electrodes), current rates of I(CS) = 18.9 mA g^{-1}, I(TCS) = 19.1 mA g^{-1}, and I(FCS) = 18.6 mA g^{-1} were chosen for GDC interruptions, corresponding to an uptake or release of 8 Na/MCr_2S_4 (Eq. 1) in 40 h (C/40). CV curves (film electrodes) were recorded in the potential range 3.0–0.1 V with a scan rate $v = 0.1$ mV s^{-1} on a Biologic VSP potentiostat.

Material characterizations

Initial characterization of pristine samples was carried out by in-house XRPD (PANalytical Empyrean diffractometer with PIXcel 1D detector, Cu-K_α radiation, Debye–Scherrer geometry), energy-dispersive X-ray spectroscopy (EDX) and scanning electron microscopy (SEM) (Zeiss Gemini Ultra-55Plus with Oxford SD detector), and elemental analysis (Elementar vario MICRO Cube). The final pristine products and ex situ samples, obtained at distinct GDC interruption points, were packed in glass capillaries ($d = 0.7$ mm, Hilgenberg, Germany) in an Ar-filled glovebox and sealed with beeswax. High-energy (~ 60 keV) synchrotron-based experiments were performed at beamline P02.1, PETRA III (DESY, Hamburg): XRPD patterns and total scattering data were collected in Debye–Scherrer geometry at a wavelength of λ(CS) = λ(TCS) = 0.20703 Å and λ(FCS) = 0.20697 Å utilizing a Perkin Elmer XRD1621 amorphous silicon area detector placed at sample to detector distances of 1015(1) mm (XRPD) and 356(1) mm (total scattering). For calibration, to account for instrumental line broadening (XRPD) and for Q-damping (PDF), LaB_6 (NIST 660b) was measured as standard applying the same conditions. An empty capillary was measured to subtract glass contributions from the total scattering patterns. Raw data processing was performed with DAWN Science [72] and total scattering data were transformed into atomic PDFs, $G(r)$, applying $Q_{max} = 24$ Å^{-1} using xPDFsuite [73]. Joint refinements of XRPD and PDF data were performed for the pristine samples using Topas Academic v6 [74, 75]. For the XRPD patterns, 9th order polynomial functions were applied to model backgrounds and Thompson-Cox-Hasting pseudo-Voigt profiles to contribute for instrumental line broadening [76]. For the PDF data, pseudo-Voigt Q-damping functions were applied to account for instrumental parameters and spherical peak shape functions with lower cutoff were used to consider the transition from correlated (small r values) to uncorrelated (high r values) atomic motion. Lattice parameters, atomic positions, Debye–Waller (DW) factors, and site occupancy factors (SOF) were co-refined during global optimization applying a weighting scheme such that parts of χ^2 were about equal for the XPRD and PDF data sets [77, 78]. Special coordinates and SOFs of S atoms were fixed during the refinements. ICSD structure data were used for simulation of reference patterns and for starting parameters of the refinements: Cr_3S_4 (ICSD-16722), $TiCr_2S_4$ (ICSD-42907), $FeCr_2S_4$ (ICSD-625938), Cr_2O_3 (ICSD-25781), Na_2S (ICSD-644959), bcc-Cr (ICSD-64711), bcc-Fe (ICSD-64795), and hcp-Ti (ICSD-43416).

Results and discussion

Characterization of pristine compounds

The stoichiometry was determined by EDX yielding compositions of $Cr_{3.00(6)}S_{4.00(6)}$, $Ti_{0.99(9)}Cr_{2.04(8)}S_{3.97(6)}$, and $Fe_{0.98(2)}Cr_{2.03(7)}S_{3.99(9)}$ in line with nominal values (Table S1 and Fig. S1). Further elemental analysis demonstrates good agreement of the S content in all compounds with expected values (Table S2). The layered nature of CS and TCS is

clearly visible in the SEM images, whereas the product FCS exhibits no specific particle shape morphology (Fig. S2).

In accordance to literature, the compounds CS and TCS crystallize in the monoclinic SG $I12/m1$, whereas FCS crystallizes in the cubic SG $Fd\bar{3}m$ (cf. "Introduction"). This is evidenced by joint Rietveld-like least-squares refinements of XRPD and PDF data yielding good agreement of the averaged long-range structure and local order for all compounds (Fig. 2, structural parameters in Table 1). For CS, minute amounts of Cr_2O_3 (≈ 1.0 wt%) were detected,

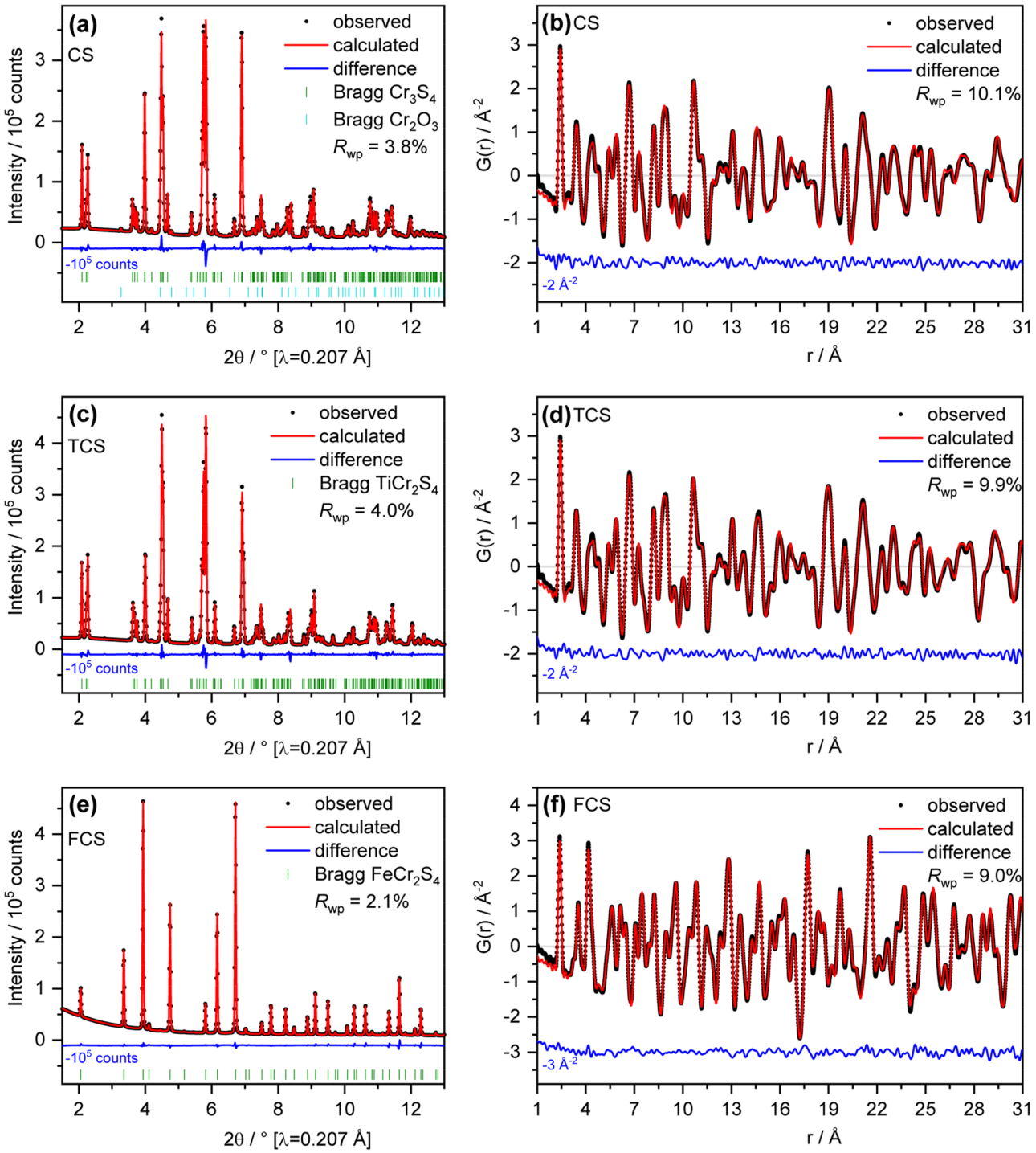

Fig. 2 Results of joint Rietveld-like least-squares XRPD-PDF refinements: **a**, **c**, and **e** XRPD patterns for CS, TCS, and FCS, respectively, each co-refined with corresponding PDFs shown in **b**, **d**, and **f**. Details are listed in Table 1

Table 1 Structural parameters co-refined from XRPD and PDF for **a** CS, **b** TCS, and **c** FCS at room temperature. Estimated standard deviations are given in parentheses

Atom	WP[a]	*x*	*y*	*z*	DW[b](Å^2)	SOF[c]
(a) CS (Cr_3S_4); impurities: 1.0 wt% Cr_2O_3; R_{wp} (XRPD) = 3.8%, R_{wp} (PDF) = 10.1% SG: *I*12/*m*1; *a* = 5.9682(1) Å, *b* = 3.4308(1) Å, *c* = 11.3252(2) Å, *β* = 91.295(1)						
Cr1	2*a*	0.0	0.0	0.0	0.73(3)	0.09(1)
Cr2	2*c*	0.0	0.0	0.5	0.73(3)	0.98(1)
Cr3	4*i*	0.0201(1)	0.0	0.2418(1)	0.68(2)	0.98(1)
S1	4*i*	0.3389(3)	0.0	0.8649(1)	0.77(2)	1.0
S2	4*i*	0.3314(3)	0.0	0.3785(1)	0.73(3)	1.0
(b) TCS ($TiCr_2S_4$); R_{wp} (XRPD) = 4.0%, R_{wp} (PDF) = 9.9% SG: *I*12/*m*1; *a* = 5.9618(1) Å, *b* = 3.4115(1) Å, *c* = 11.3573(2) Å, *β* = 91.292(1)						
Cr1/Ti1	2*a*	0.0	0.0	0.0	0.76(3)	0.00(1)
Cr2/Ti2	2*c*	0.0	0.0	0.5	0.76(3)	1.00(1)
Cr3/Ti3	4*i*	0.0226(1)	0.0	0.2416(1)	0.62(2)	0.99(1)
S1	4*i*	0.3389(2)	0.0	0.8679(1)	0.67(2)	1.0
S2	4*i*	0.3324(3)	0.0	0.3816(1)	0.77(2)	1.0
(c) FCS ($FeCr_2S_4$); R_{wp} (XRPD) = 2.1%, R_{wp} (PDF) = 9.0% SG: $Fd\bar{3}m$; *a* = 9.9953(1) Å						
Fe	8*a*	0.0	0.0	0.0	0.77(1)	1.00(1)
Cr	16*d*	0.125	0.125	0.125	0.73(3)	1.00(1)
S	32*e*	0.3845(1)	0.3845(1)	0.3845(1)	0.72(1)	1.0

[a] *WP* Wyckoff position

[b] *DW* Debye Waller factor

[c] *SOF* site occupancy factor

presumably resulting from reaction of Cr with the quartz ampoule. Moreover, the refinement reveals the presence of about 3% Cr atoms on Wyckoff position 2*a*, which represents the empty octahedral sites in the ideal Cr_3S_4 structure type (Table 1). Lattice parameters and atomic fractional coordinates are in good agreement with previous results reported for this compound [79]. For TCS, it is not possible to distinguish between Ti and Cr via XRPD; hence, both elements are refined together (Fig. 2c, d). In contrast to CS, no atoms are located on site 2*a* in TCS (Table 1). For the joint XRPD-PDF refinement of FCS (Fig. 2e, f), the positions of Fe and Cr were fixed to tetrahedral and octahedral sites, respectively (cf. "Introduction"). The results for TCS and FCS demonstrate phase-pure products and yield structural parameters in accordance to values reported for TCS [65, 79] and FCS [66, 80–85].

Electrochemical properties in SIBs

GDC (Fig. 3a, b) and CV (Fig. 3c, d) profiles were recorded during the 1st, 2nd, and 5th cycle using film electrodes in Na half-cells. The main electrochemical features are summarized in Table 2. During initial discharge of the CS electrode, one pronounced pseudo-plateau is visible around 0.41 V (GDC, Fig. 3a), which corresponds to a narrow cathodic peak in the 1st CV cycle (Fig. 3c). Although the capacities during the 1st discharge (8.0 Na/CS, CV; 8.3 Na/CS, GDC) match with the expected value for ideal conversion (8.0 Na/CS, cf. Eq. 1), contributions of chemical side-reactions and formation of a solid electrolyte interphase (SEI) must be considered. Thus, a full conversion reaction of CS is hindered applying the selected conditions, which will be further discussed in the next chapter. Irreversible redox reactions of Cr^{3+} cations and SEI formation cause an irreversible capacity loss of 30% in the 1st GDC cycle close to values reported for $Na/CuCrS_2$ (33%) [21], $Na/NiCr_2S_4$ (28%) [22], and Na/CuV_2S_4 (27.5%) [86], where very similar cell and electrode conditions were applied. One pronounced, peak is observed in the subsequent cathodic and anodic CV curves (Fig. 3c, d and Table 2) demonstrating that a single, reversible redox event between Cr^{x+} cations and Cr^0 accounts for the high capacities obtained after the 1st GDC and CV cycle (capacities fade < 2%, cf. Table 2). Almost equal capacities are delivered during subsequent cycles and correspond to ≈ 6 Na/CS uptake and release. Hence, the redox reaction in Eq. (2) most likely occurs:

$$3\ Cr^0 + 6\ Na^+ \rightleftharpoons 3\ Cr^{2+} + 6\ Na^0 \quad (2)$$

Discharging the FCS electrode in the 1st cycle yields a pronounced pseudo-plateau at 0.43 V (GDC, Fig. 3a), which corresponds to the narrow cathodic CV peak at 0.36 V (Fig. 3c). Both electrochemical features are comparable to those observed for CS but higher discharge capacities are achieved (9.3 Na/FCS, CV; 9.7 Na/CS, GDC). Thus, a full conversion reaction (Eq. 1) occurs in addition to SEI

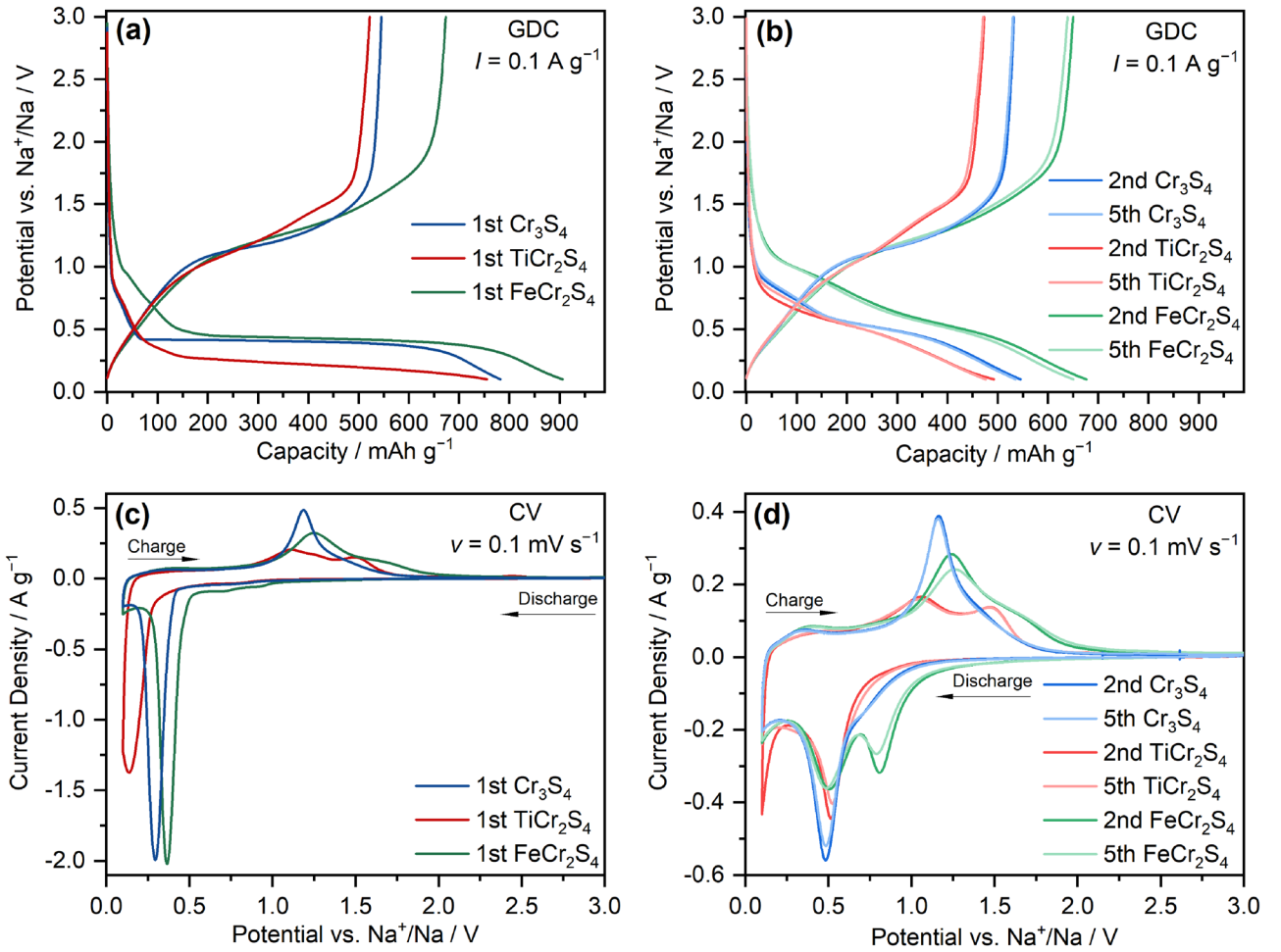

Fig. 3 Electrochemical properties of Na/CS (blue), Na/TCS (red), and Na/FCS (green) test cells in the potential window 3.0–0.1 V: GDC profiles in the **a** 1st, **b** 2nd, and 5th cycle applying a current density of 0.1 A g^{-1}; CV curves in the **c** 1st, **d** 2nd, and 5th cycle applying a scan rate of 0.1 mV s^{-1}

Table 2 Main redox events, capacities and corresponding Na uptake/release observed during the 1st, 2nd, and 5th cycle of GDC (I=0.1 A g^{-1}) and CV (v=0.1 mV s^{-1}) measurements for Na/CS, Na/TCS, and Na/FCS cells. GDC potentials were extracted using differential capacity dQ/dV analysis of respective curves in Fig. 3a, b, whereas CV capacities were calculated by integration of respective curves in Fig. 3c, d

	Cycle no	Redox potentials *vs.* Na^+/Na (V)				Capacity (mAh g^{-1}); Na uptake/release (x Na^+)			
		Discharge		Charge		Discharge		Charge	
		GDC	CV	GDC	CV	GDC	CV	GDC	CV
CS	1	0.41 (vs)	0.29 (vs)	1.15 (s)	1.19 (s)	782; 8.3	754; 8.0	545; 5.8	558; 5.9
	2	0.51 (s)	0.48 (s)	1.13 (s)	1.16 (s)	545; 5.8	558; 5.9	532; 5.6	554; 5.9
	5	0.51 (s)	0.48 (s)	1.13 (s)	1.16 (s)	536; 5.7	547; 5.8	530; 5.6	551; 5.8
TCS	1	0.22 (vs)	0.14 (vs)	1.10 (m), 1.49 (m)	1.11 (m), 1.50 (m)	755; 7.9	652; 6.8	522; 5.5	470; 4.9
	2	0.54 (s)	0.51 (s), < 0.1	1.10 (m), 1.48 (m)	1.06 (m), 1.48 (m)	492; 5.1	483; 5.1	474; 5.0	462; 4.8
	5	0.54 (s)	0.52 (s)	1.18 (m), 1.47 (m)	1.05 (m), 1.47 (m)	476; 5.0	469; 4.9	471; 4.9	468; 4.9
FCS	1	0.43 (vs)	0.36 (vs)	1.25 (s), ~ 1.6 (sh)	1.25 (s), ~ 1.6 (sh)	906; 9.7	867; 9.3	674; 7.2	658; 7.1
	2	0.53 (s), 0.97 (m)	0.51 (s), 0.81 (s)	1.19 (s), ~ 1.6 (sh)	1.24 (s), ~ 1.6 (sh)	676; 7.3	668; 7.2	650; 7.0	649; 7.0
	5	0.53 (s), 1.00 (m)	0.49 (s), 0.79 (m)	1.19 (s), ~ 1.6 (sh)	1.26 (s), ~ 1.6 (sh)	650; 7.0	638; 6.9	639; 6.9	640; 6.9

Peak labels are given in round parentheses: *w* weak, *m* medium, *s* strong, *vs* very strong, *sh* shoulder

formation leading to an irreversible capacity loss of 26% during the 1st cycle. In contrast to CS, two cathodic peaks and two less resolved anodic events are observed in subsequent CV cycles (Fig. 3c, d and Table 2). This observation strongly indicates that Fe and Cr both participate in the redox reactions. The reversible capacities obtained in the 2nd to 5th GDC and CV cycles (capacities fade < 5%, cf. Table 2) correspond to a shuttle of ≈ 7 Na/FCS. Taking also the observations for CS into account (Eq. 2), a redox reaction according to Eq. (3) may be formulated for FCS:

$$Fe^0 + 2\ Cr^0 + 7\ Na^+ \rightleftharpoons Fe^{3+} + 2\ Cr^{2+} + 7\ Na^0 \quad (3)$$

The lowest reduction voltage of the three metal sulfides during the initial discharge is observed for TCS, also exhibiting a less distinct pseudo-plateau (GDC, Fig. 3a) and a broader cathodic CV peak (Fig. 3c) compared to CS and FCS. This point towards a higher internal resistance for the TCS electrodes resulting in a larger polarization voltage. The conversion process of TCS is obviously incomplete if discharged to 0.1 V, clearly evidenced by the interruption at $V_{low} = 0.1$ V of the cathodic event (1st CV curve, Fig. 3c). This is further confirmed by the initial discharge capacities (6.8 Na/TCS, CV; 7.9 Na/TCS, GDC), which is smaller than expected (Eq. 1). Again, additional contributions from SEI formation and chemical side-reactions need to be considered, in particular because the irreversible capacity loss (31%, TCS) during the 1st GDC cycle is close to the findings for CS and FCS. During subsequent GDC and CV cycles, the TCS electrodes deliver the smallest capacities of the three sulfides (Table 2) and ≈ 5 Na/TCS are reversibly shuttled (capacity fade < 4%). The incomplete reduction in the 1st cycle also causes a cathodic peak located at 0.1 V in the 2nd CV cycle (Fig. 3d). In contrast to the results for CS, two anodic CV signals are clearly visible for TCS indicating that both metal centers, Ti and Cr, participate in the redox reactions. We note that the reduction of Ti cations to elemental state was recently observed during discharge of TiO_2 [87] and TiS_2 [88] anodes. However, only one cathodic CV signal occurs after the 1st cycle for TCS. The area of the one cathodic CV peak corresponds to the sum of the two anodic CV peak areas; thus, the reduction of Ti and Cr cations seems to occur at a similar voltage vs. Na^+/Na. However, a distinct assignment of electrochemical features to redox pairs remains speculative for TCS.

GDC performance tests were conducted for all electrode materials to evaluate long-term (Fig. 4a and Table 3) and rate stabilities (Fig. 4b and Table 4). Applying a current rate of 0.5 A g^{-1} after the 1st cycle ($I_{1st} = 0.1$ A g^{-1}), all electrodes deliver high capacities for 200 cycles accompanied by Coloumbic Efficiencies > 99% after the 5th cycle. The highest capacities are observed for FCS but it decreases by 14% (to 524 mAh g^{-1} ≈ 5.6 Na/FCS) until the 200th cycle. These high capacities can be explained by an almost full conversion reaction as discussed further below (XRPD and PDF analyses). In contrast, CS exhibits the best long-term stability and 5.0 Na/CS (470 mAh g^{-1}) are reversibly shuttled after 200 cycles corresponding to a superior capacity retention of 93%. As evidences further below (XRPD and PDF analyses), the crystalline material CS is completely decomposed to X-ray amorphous products during sodiation and insulating Na_2S does not crystallize, which boosts the long-term stability. Although the TCS electrode delivers the lowest capacities during cycling, e.g., 375 mAh g^{-1} (≈ 3.9 Na/TCS, capacity retention: 85%) after 200 cycles, this electrode offers the best rate capability in SIBs comparing the three sulfides. For example, the TCS electrode still delivers 264 mAh g^{-1} (≈ 2.8 Na/TCS, capacity retention: 58%) at a

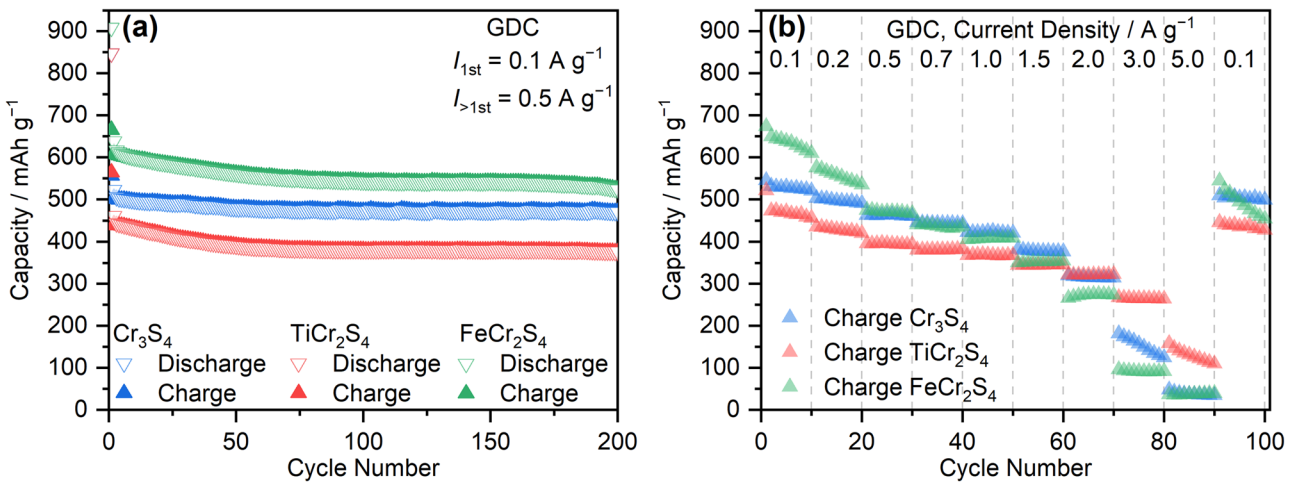

Fig. 4 GDC performance tests of Na/CS (blue), Na/TCS (red), and Na/FCS (green) test cells in the potential window 3.0–0.1 V: **a** long-term stability tests applying a current density of 0.5 A g^{-1} (1st cycle: $I = 0.1$ A g^{-1}) and **b** charge capacities of rate capability tests

Table 3 Results of long-term stability tests ($I = 0.5$ A g^{-1}): charge capacities after several cycles for Na cells using CS, TCS, and FCS electrodes. Results for $NiCr_2S_4$ electrodes are shown for comparison. The capacity retention is related to the capacity of the 2nd cycle

Cycle number	**CS**		**TCS**		**FCS**		**$NiCr_2S_4$** [22]	
	Capacity (mAh g^{-1})	Capacity retention (%)	Capacity (mAh g^{-1})	Capacity retention (%)	Capacity (mAh g^{-1})	Capacity retention (%)	Capacity (mAh g^{-1})	Capacity retention (%)
2	504	100	441	100	611	100	593	100
10	490	97	431	98	597	98	581	98
50	479	95	390	88	562	92	548	92
100	473	94	379	86	543	89	539	91
150	472	94	379	86	542	89	553	93
200	470	93	375	85	524	86	558	94

current rate of 3.0 A g^{-1}, whereas the charge storage at this high rate is significantly worse using CS (125 mAh g^{-1} ≈ 1.3 Na/CS, capacity retention: 24%) or FCS (92 mAh g^{-1} ≈ 1.0 Na/FCS, capacity retention: 15%). The poor rate performance of the CS and FCS electrodes might result from diffusion limiting processes at higher current rates, but detailed studies about the reaction kinetics are necessary in future work. Comparing the overall performance of MCr_2S_4 electrodes (rate capability, cycle life, and magnitude of capacity, cf. Tables 3 and 4), $NiCr_2S_4$ offers the best electrochemical properties [22].

Structural changes during the 1st GDC cycle

The sodium storage mechanisms during the 1st GDC cycle were investigated at selected interruption points (Fig. 5) by high-energy XRPD (Fig. 6) and PDF (Fig. 7) analyses. Ex situ samples were collected using pellet electrodes. A comparison (Fig. S3) of the initial galvanostatic discharge profiles to 0.1 V using common film electrodes with and pellet electrodes without PVDF (cf. "Experimental") demonstrates that smaller capacities are obtained (≈ 6.8 Na/CS, ≈ 6.0 Na/TCS, and ≈ 7.3 Na/FCS) for the latter. This is not surprising since (i) PVDF contributes to SEI formation in SIBs, i.e., additional Na is consumed by decomposition of PVDF into NaF [22, 89–91] and (ii) different cell conditions influence the electrochemical kinetics, i.e. the electron and Na^+ ion diffusion. Thus, we selected a potential window of 3.0–0.01 V (Fig. 5), also because the former electrochemical experiments indicated that the full conversion is incomplete for CS and TCS at $V = 0.1$ V. Even so, the capacities obtained by discharging the pellet electrodes to 0.01 V (Fig. 5) demonstrate full conversion only for FCS (≈ 8.0 Na/FCS) and incomplete conversion for CS and TCS (≈ 7.4 Na/CS, ≈ 7.1 Na/TCS).

The results from XRPD (Fig. 6, cf. Figs. S4, S5 and S6) evidence that the sodium insertion–transition metal extrusion mechanism found for $CuCrS_2$ [21] and $NiCr_2S_4$ [22]

Table 4 Results of rate capability tests: charge capacities after every 10th cycle for Na cells using CS, TCS, and FCS electrodes. Results for $NiCr_2S_4$ electrodes are shown for comparison. The capacity retention is related to the capacity of the 10th cycle applying the 1st rate

Current density (A g^{-1})	**CS**		**TCS**		**FCS**		**$NiCr_2S_4$** [22]	
	Capacity (mAh g^{-1})	Capacity retention (%)	Capacity (mAh g^{-1})	Capacity retention (%)	Capacity (mAh g^{-1})	Capacity retention (%)	Capacity (mAh g^{-1})	Capacity retention (%)
0.1	521	100	456	100	610	100	612	100
0.2	491	94	420	92	536	88	579	95
0.5	460	88	393	86	467	77	550	90
0.7	443	85	382	84	436	71	534	87
1	420	81	367	80	409	67	521	85
1.5	376	72	345	76	354	58	505	83
2	314	60	323	71	273	45	492	80
3	125	24	264	58	92	15	468	76
5	35	7	110	24	39	6	399	65
0.1	499	96	427	94	454	74	583	95

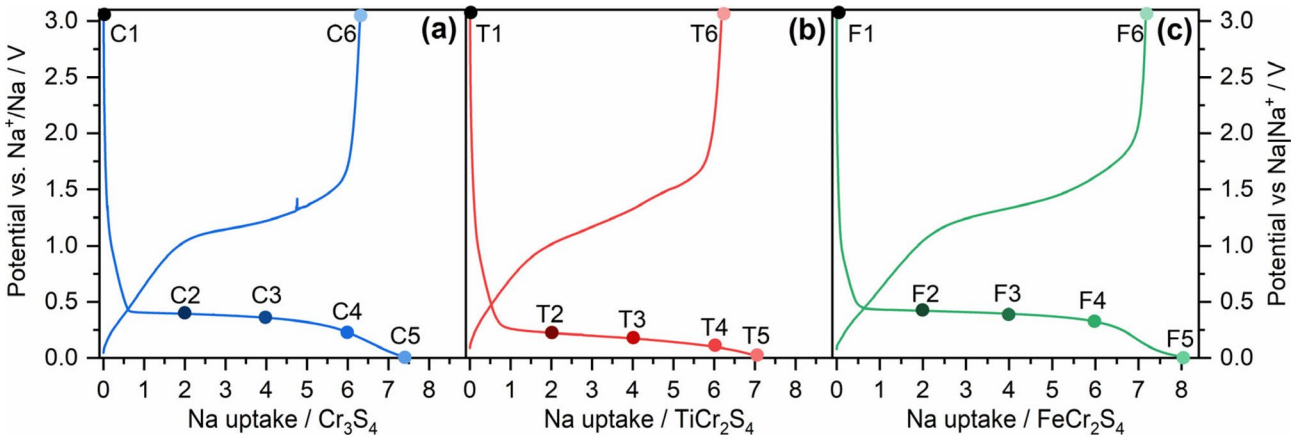

Fig. 5 GDC profiles using pellet electrodes in Na cells for **a** CS, **b** TCS, and **c** FCS. The interruption points for ex situ investigations are marked with M1–M6 (M = C, T, and F)

is not applicable to CS, TCS and FCS: During discharge, neither formation of nanocrystalline metals is observed nor reflections related to an intermediate $NaCrS_2$-phase appear. During uptake of 6 Na per formula unit (C4, T4, and F4 in Fig. 6), the reflection intensities of the educts successively decrease. For CS, these reflections completely vanish at 6 Na/CS and two small reflections at ≈ 4.63° and ≈ 6.66° 2θ appear (marked with asterisks in Fig. 6a). They cannot be related to any known phases with compositions including Cr, S, and Na but indicate the formation of an intermediate at this point. Very small reflections, which does not change for the CS XRPD series (marked with "x" in Fig. 6a), correspond to the Cr_2O_3 impurity already detected in the pristine material, not taking part in Na storage as an electric isolator [92]. Even after discharge to 0.01 V (C5), XRPD does not yield distinct evidence for the formation of nanoscopic Na_2S or for crystalline, elemental Cr. However, very broad signals around ≈ 5.6° 2θ and ≈ 9.7° 2θ may be caused by ultra-small, X-ray amorphous Cr particles (cf. Fig. S4). The charged sample (C6) contains only X-ray amorphous products (besides crystalline Cr_2O_3). These findings are typical phenomena reported for conversion-type materials. For TCS,

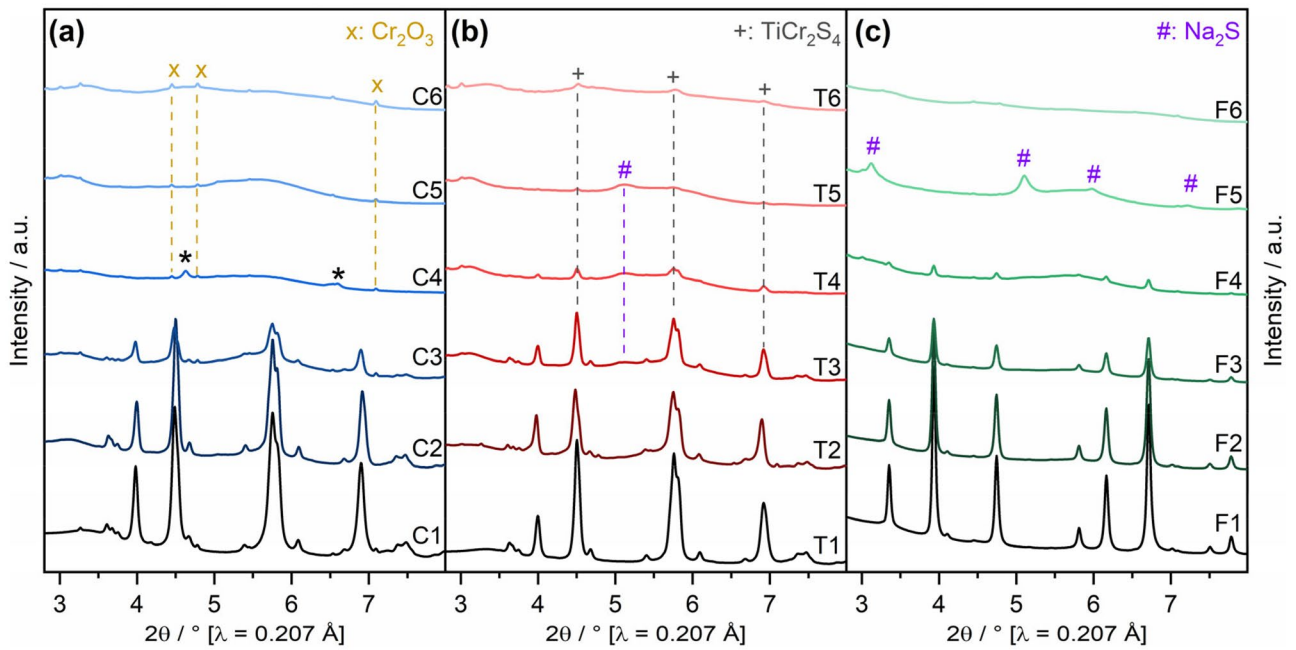

Fig. 6 Evolution of XRPD patterns collected at interruption points M1–M6 (M = C, T, and F; cf. Fig. 5) for **a** CS, **b** TCS, and **c** FCS pellet electrodes during the 1st GDC cycle

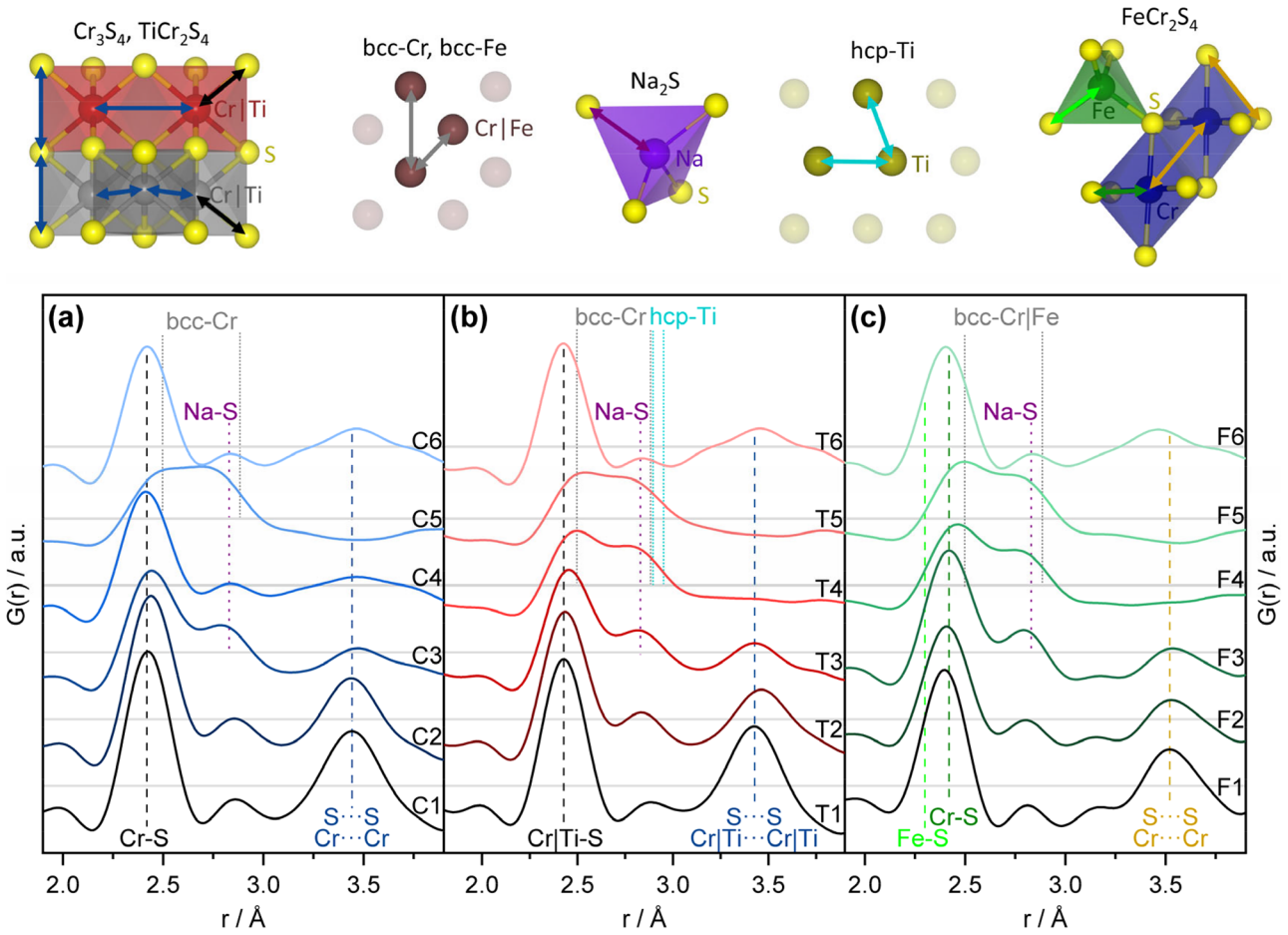

Fig. 7 Evolution of PDFs corresponding to the interruption points M1–M6 (M = C, T, and F; cf. Fig. 5) for **a** CS, **b** TCS, and **c** FCS pellet electrodes during the 1st GDC cycle. Vertical color lines represent main, averaged interatomic connections expected in crystalline MCr_2S_4 (M = Cr, Fe, and Ti: M-S, S···S and M···M), Na_2S (Na-S), hcp-Ti, bcc-Cr, and bcc-Fe. The color labels correspond to the separations in the local environments of expected products shown at the top. Chemical structures were created with Vesta v3 [71]

a comparable picture is obtained including a charge storage mechanism via generation of X-ray amorphous conversion products (Figs. 6e and S5). The formation of nanocrystalline Na_2S is observed between 4 and 7 Na/TCS (T3–T5). At 6 Na/TCS (T4, $V \approx 0.1$ V), pronounced reflections of the starting material are still detected. These reflections remain after uptake of 7 Na/TCS (T5) and after a full cycle (T6) with smaller scattering intensity, unambiguously demonstrating the incomplete conversion at the selected conditions for TCS. This explains the lower capacities detected for TCS in all electrochemical GDC and CV tests compared to CS and FCS. Also during discharge of the FCS electrode, neither crystalline elemental Fe nor Cr is observed (Figs. 6f and S6). The formation of nanocrystalline Na_2S is, on the contrary, clearly evidenced after an uptake of 8 Na/FCS (F5), and the charge product (F6) is again X-ray amorphous. More distinct reflections for Na_2S at full discharge are a good hint that the conversion of FCS is in an advanced state after full discharge compared to CS and TCS, which explains the higher capacities observed during GDC and CV tests for Na/FCS cells. The crystallization of an insulating Na_2S matrix observed for FCS and TCS is accompanied by additional volume expansion, forcing the contacts between X-ray amorphous products and the electric conductor to break. This explains the worse capacity retention observed for FCS and TCS during long-term cycling (Fig. 4 and Table 3) compared to CS.

Atomic PDFs corresponding to the samples M1–M6 of CS, TCS, and FCS are shown in Fig. 7, representing the evolution in the averaged local environments (1.9–3.9 Å) during Na uptake and release (cf. Fig. S7 for $r = 1$ to 21 Å). In agreement with the observations from XRPD, a look at the mid-range order (Fig. S7) confirms that all samples lose their structural integrity and barely any total scattering intensity is observed at $r > 7$ Å after uptake of 6 Na per formula unit (M4–M6). Hence, only very small conversion products account for the charge storage properties after initial structural disintegration. Total scattering intensities

corresponding to M–S (M = Cr, Ti, Fe) bonds decrease during all initial discharge processes (Fig. 7). In addition, very short interatomic separations M···M and S···S, which are apparent in the pristine compounds MCr_2S_4, completely disappear after discharging to 0.01 V (for TCS and FCS already at 6 Na/MCS). Thus, these conversion products are not related to the pristine materials, but after charging the electrodes to 3.0 V (M6), PDF peaks reappear in the short range at very similar positions as observed for the pristine compounds. Hence, the local environments of the charged products resemble that expected for very small metal sulfides. Because the charge products lost their structural integrity in the mid- to long-range order, a relation to particular sulfidic phases is obviously speculative. The PDFs of all discharged samples (V = 0.01 V, M5) are comparable to each other and point towards the formation of Na–S bonds as well as metal–metal separations in the elemental metals. However, differentiation between PDF signals corresponding to similar bonds in the first shells of bcc-Cr, bcc-Fe, and hcp-Ti is not possible because the PDFs represent histograms of all interatomic distances in the sample. Representatively, PDFs and XRPD patterns corresponding to the discharged and charged state of FCS electrodes in the 2nd cycle are shown in Fig. S8. Although no reflections of Na_2S are visible in the XRPD pattern after the 2nd discharge, the local environments in both discharged products (1st and 2nd cycle) are very similar as the PDFs are almost superimposable. Also, the PDFs and XRPD patterns of the charged samples in the 1st and 2nd cycle are very similar evidencing a high reversibility of the charge storage mechanism involving very small conversion products.

Conclusion

In this comparative study, the three highly crystalline chromium sulfides Cr_3S_4 (CS), $TiCr_2S_4$ (TCS), and $FeCr_2S_4$ (FCS) were analyzed as anode materials in SIBs for the first time. Galvanostatic and voltammetric investigations provide insights into the Na storage properties and extend the overall picture for sulfidic SIB-anodes. The three metal sulfides offer good long-term stability with high capacity retention between 0.1 and 3.0 V and deliver remarkably high capacities even after 200 cycles at 0.5 A g^{-1}. From the results of CV, we propose reversible redox reactions (Eqs. 2 and 3) for discharge and charge processes after the 1st cycle. Moreover, analyses of high-energy X-ray diffraction patterns and pair distribution functions provide a fundamental understanding of structural changes during the 1st cycle. In contrast to the Na insertion–Cu/Ni extrusion mechanisms observed for $CuCrS_2$ [21] and $NiCr_2S_4$ [32], neither crystalline $NaCrS_2$-like intermediates nor crystalline Cr, Ti, or Fe is formed during discharge of Na/CS, Na/TCS, or Na/FCS cells. During Na uptake, these metal sulfides are directly decomposed into X-ray amorphous conversion products embedded in a nanocrystalline Na_2S matrix, and structural integrity of the sulfides is not recovered during Na release. We conclude that the charge storage reactions occur on a very small nanoscale for the three title compounds and rather depend on the metals redox activity than on the structure of the starting compounds.

Supplementary Information The online version contains supplementary material available at https://doi.org/10.1007/s10008-022-05246-3.

Acknowledgements Financial support by the State of Schleswig-Holstein is gratefully acknowledged. We acknowledge DESY (Hamburg, Germany), a member of the Helmholtz Association HGF, for providing experimental facilities at PETRA III, beamline P02.1 (proposal BAG-20170560). We also kindly thank Christin Szillus for SEM operation and EDX evaluation.

Funding Open Access funding enabled and organized by Projekt DEAL.

Declarations

Conflict of interest The authors declare no competing interest.

References

1. Armand M, Tarascon J-M (2008) Building better batteries. Nature 451:652–657. https://doi.org/10.1038/451652a
2. Goodenough JB, Park K-S (2013) The Li-ion rechargeable battery: a perspective. J Am Chem Soc 135:1167–1176. https://doi.org/10.1021/ja3091438
3. Yang Y, Okonkwo EG, Huang G, Xu S, Sun W, He Y (2021) On the sustainability of lithium ion battery industry – a review and perspective. Energy Storage Materials 36:186–212. https://doi.org/10.1016/j.ensm.2020.12.019
4. Ziegler MS, Trancik JE (2021) Re-examining rates of lithium-ion battery technology improvement and cost decline. Energy Environ Sci 14:1635–1651. https://doi.org/10.1039/D0EE02681F
5. Slater MD, Kim D, Lee E, Johnson CS (2013) Sodium-ion batteries. Adv Funct Mater 23:947–958. https://doi.org/10.1002/adfm.201200691
6. Yang X, Rogach AL (2020) Anodes and sodium-free cathodes in sodium ion batteries. Adv Energy Mater 10:2000288. https://doi.org/10.1002/aenm.202000288

7. Tarascon J-M (2020) Na-ion versus Li-ion batteries: complementarity rather than competitiveness. Joule 4:1616–1620. https://doi.org/10.1016/j.joule.2020.06.003
8. Lee JM, Singh G, Cha W, Kim S, Yi J, Hwang S-J, Vinu A (2020) Recent advances in developing hybrid materials for sodium-ion battery anodes. ACS Energy Lett 5:1939–1966. https://doi.org/10.1021/acsenergylett.0c00973
9. Fang Y, Xiao L, Chen Z, Ai X, Cao Y, Yang H (2018) Recent advances in sodium-ion battery materials. Electrochem Energ Rev 1:294–323. https://doi.org/10.1007/s41918-018-0008-x
10. Fang Y, Luan D, Lou XW (2020) Recent advances on mixed metal sulfides for advanced sodium-ion batteries. Adv Mater 32:2002976. https://doi.org/10.1002/adma.202002976
11. Jache B, Adelhelm P (2014) Use of graphite as a highly reversible electrode with superior cycle life for sodium-ion batteries by making use of co-intercalation phenomena. Angew Chem Int Ed 53:10169–10173. https://doi.org/10.1002/anie.201403734
12. Nobuhara K, Nakayama H, Nose M, Nakanishi S, Iba H (2013) First-principles study of alkali metal-graphite intercalation compounds. J Power Sources 243:585–587. https://doi.org/10.1016/j.jpowsour.2013.06.057
13. Sangster J (2007) C-Na (carbon-sodium) system. J Phase Equilib Diff 28:571–579. https://doi.org/10.1007/s11669-007-9194-7
14. Cabana J, Monconduit L, Larcher D, Palacín MR (2010) beyond intercalation-based Li-ion batteries: the state of the art and challenges of electrode materials reacting through conversion reactions. Adv Mater 22:E170–E192. https://doi.org/10.1002/adma.201000717
15. Zhang H, Hasa I, Passerini S (2018) Beyond insertion for Na-ion batteries: nanostructured alloying and conversion anode materials. Adv Energy Mater 8:1702582. https://doi.org/10.1002/aenm.201702582
16. Nam K-H, Hwa Y, Park C-M (2020) Zinc phosphides as outstanding sodium-ion battery anodes. ACS Appl Mater Interfaces 12:15053–15062. https://doi.org/10.1021/acsami.9b21803
17. Fullenwarth J, Darwiche A, Soares A, Donnadieu B, Monconduit L (2014) NiP3: a promising negative electrode for Li- and Na-ion batteries. J Mater Chem A 2:2050–2059. https://doi.org/10.1039/C3TA13976J
18. Ha S, Kim J-K, Choi A, Kim Y, Lee KT (2014) Sodium–metal halide and sodium–air batteries. ChemPhysChem 15:1971–1982. https://doi.org/10.1002/cphc.201402215
19. Ma D, Wang H, Li Y, Xu D, Yuan S, Huang X, Zhang X, Zhang Y (2014) In situ generated FeF_3 in homogeneous iron matrix toward high-performance cathode material for sodium-ion batteries. Nano Energy 10:295–304. https://doi.org/10.1016/j.nanoen.2014.10.004
20. Klein F, Jache B, Bhide A, Adelhelm P (2013) Conversion reactions for sodium-ion batteries. Phys Chem Chem Phys 15:15876–15887. https://doi.org/10.1039/C3CP52125G
21. Krengel M, Hansen A-L, Hartmann F, van Dinter J, Bensch W (2018) Elucidation of the sodium – copper extrusion mechanism in $CuCrS_2$: a high capacity, long-life anode material for sodium-ion batteries. Batteries Supercaps 1:176–183. https://doi.org/10.1002/batt.201800039
22. Hartmann F, Etter M, Cibin G, Liers L, Terraschke H, Bensch W (2021) Superior sodium storage properties in the anode material $NiCr_2S_4$ for sodium-ion batteries: an X-ray diffraction, pair distribution function, and X-ray absorption study reveals a conversion mechanism via nickel extrusion. Adv Mater 33:2101576. https://doi.org/10.1002/adma.202101576
23. Tan H, Feng Y, Rui X, Yu Y, Huang S (2020) Metal chalcogenides: paving the way for high-performance sodium/potassium-ion batteries. Small Methods 4:1900563. https://doi.org/10.1002/smtd.201900563
24. Liu P, Han J, Zhu K, Dong Z, Jiao L (2020) Heterostructure $SnSe_2$ /ZnSe@PDA nanobox for stable and highly efficient sodium-ion storage. Adv Energy Mater 10:2000741. https://doi.org/10.1002/aenm.202000741
25. Gu M, Kushima A, Shao Y, Zhang J-G, Liu J, Browning ND, Li J, Wang C (2013) Probing the failure mechanism of sno_2 nanowires for sodium-ion batteries. Nano Lett 13:5203–5211. https://doi.org/10.1021/nl402633n
26. van Dinter J, Synnatschke K, Engesser TA, Indris S, Wolff N, Gronenberg O, Etter M, Cibin G, Kienle L, Backes C, Bensch W (2020) What happens structurally and chemically during sodium uptake and release by $Ni_2P_2S_6$: a combined X-ray diffraction, X-ray absorption, pair distribution function and MAS NMR analysis. J Mater Chem A 8:22401–22415. https://doi.org/10.1039/D0TA07889A
27. Li W, Song Q, Li M, Yuan Y, Zhang J, Wang N, Yang Z, Huang J, Lu J, Li X (2021) Chemical heterointerface engineering on hybrid electrode materials for electrochemical energy storage. Small Methods 5:2100444. https://doi.org/10.1002/smtd.202100444
28. Shadike Z, Zhou Y-N, Ding F, Sang L, Nam K-W, Yang X-Q, Fu Z-W (2014) The new electrochemical reaction mechanism of Na/FeS_2 cell at ambient temperature. J Power Sources 260:72–76. https://doi.org/10.1016/j.jpowsour.2014.03.011
29. Walter M, Zünd T, V. Kovalenko M, (2015) Pyrite (FeS_2) nanocrystals as inexpensive high-performance lithium-ion cathode and sodium-ion anode materials. Nanoscale 7:9158–9163. https://doi.org/10.1039/C5NR00398A
30. Wang Q, Guo C, Zhu Y, He J, Wang H (2018) Reduced graphene oxide-wrapped FeS_2 composite as anode for high-performance sodium-ion batteries. Nano-Micro Lett 10:30. https://doi.org/10.1007/s40820-017-0183-z
31. Qi S, Mi L, Song K, Yang K, Ma J, Feng X, Zhang J, Chen W (2019) Understanding shuttling effect in sodium ion batteries for the solution of capacity fading: FeS_2 as an example. J Phys Chem C 123:2775–2782. https://doi.org/10.1021/acs.jpcc.8b11069
32. Hartmann F, Etter M, Cibin G, Groß H, Kienle L, Bensch W (2022) Understanding sodium storage properties of ultra-small Fe_3S_4 nanoparticles – a combined XRD, PDF, XAS and electrokinetic study. Nanoscale. https://doi.org/10.1039/D1NR06950K
33. Li Q, Wei Q, Zuo W, Huang L, Luo W, An Q, Pelenovich VO, Mai L, Zhang Q (2017) Greigite Fe_3S_4 as a new anode material for high-performance sodium-ion batteries. Chem Sci 8:160–164
34. Liu Q, Gao J, Cao C, Yin G, Jiang Z, Ge M, Xiao X, Lee W-K, Wang J (2019) Insights into enhanced sodium ion storage mechanism in Fe_3S_4: the coupling of surface chemistry, microstructural regulation and 3D electronic transport. Nano Energy 62:384–392. https://doi.org/10.1016/j.nanoen.2019.05.055
35. Senkale S, Indris S, Etter M, Bensch W (2021) $CuFeS_2$ as a very stable high-capacity anode material for sodium-ion batteries: a multimethod approach for elucidation of the complex reaction mechanisms during discharge and charge processes. ACS Appl Mater Interfaces 13:26034–26045. https://doi.org/10.1021/acsami.1c04946
36. Peng S, Han X, Li L, Zhu Z, Cheng F, Srinivansan M, Adams S, Ramakrishna S (2016) Unique cobalt sulfide/reduced graphene oxide composite as an anode for sodium-ion batteries with superior rate capability and long cycling stability. Small 12:1359–1368. https://doi.org/10.1002/smll.201502788
37. Guo Q, Ma Y, Chen T, Xia Q, Yang M, Xia H, Yu Y (2017) Cobalt sulfide quantum dot embedded N/S-doped carbon nanosheets with superior reversibility and rate capability for sodium-ion batteries. ACS Nano 11:12658–12667. https://doi.org/10.1021/acsnano.7b07132
38. Zhou L, Zhang K, Sheng J, An Q, Tao Z, Kang Y-M, Chen J, Mai L (2017) Structural and chemical synergistic effect of CoS nanoparticles and porous carbon nanorods for high-performance sodium storage. Nano Energy 35:281–289. https://doi.org/10.1016/j.nanoen.2017.03.052

39. Wang J, Cao D, Yang G, Yang Y, Wang H (2017) Synthesis of NiS/carbon composites as anodes for high-performance sodium-ion batteries. J Solid State Electrochem 21:3047–3055. https://doi.org/10.1007/s10008-017-3600-9
40. Zhang D, Sun W, Zhang Y, Dou Y, Jiang Y, Dou SX (2016) Engineering hierarchical hollow nickel sulfide spheres for high-performance sodium storage. Adv Funct Mater 26:7479–7485. https://doi.org/10.1002/adfm.201602933
41. Dong C, Liang J, He Y, Li C, Chen X, Guo L, Tian F, Qian Y, Xu L (2018) $NiS_{1.03}$ hollow spheres and cages as superhigh rate capacity and stable anode materials for half/full sodium-ion batteries. ACS Nano 12:8277–8287. https://doi.org/10.1021/acsnano.8b03541
42. Zhang Z, Li Z, Yin L (2018) Hollow prism $NiCo_2S_4$ linked with interconnected reduced graphene oxide as a high performance anode material for sodium and lithium ion batteries. New J Chem 42:1467–1476. https://doi.org/10.1039/C7NJ03581K
43. Zhao M, Zhu L, Fu B, Jiang S, Zhou Y, Song Y (2019) Sodium ion storage performance of $NiCo_2S_4$ hexagonal Nanosheets. Acta Phys-Chim Sin 35:193–199. https://doi.org/10.3866/PKU.WHXB201801241
44. Miao Y, Zhao X, Wang X, Ma C, Cheng L, Chen G, Yue H, Wang L, Zhang D (2020) Flower-like $NiCo_2S_4$ nanosheets with high electrochemical performance for sodium-ion batteries. Nano Res 13:3041–3047. https://doi.org/10.1007/s12274-020-2969-4
45. Sun Z, Zhao C, Cao X, Zeng K, Ma Z, Hu Y, Tian J-H, Yang R (2020) Insights into the phase transformation of $NiCo_2S_4$@rGO for sodium-ion battery electrode. Electrochim Acta 338:135900. https://doi.org/10.1016/j.electacta.2020.135900
46. Li W, Kheimeh Sari HM, Li X (2020) Emerging layered metallic vanadium disulfide for rechargeable metal-ion batteries: progress and opportunities. Chemsuschem 13:1172–1202. https://doi.org/10.1002/cssc.201903081
47. Shadike Z, Zhou Y-N, Chen L-L, Wu Q, Yue J-L, Zhang N, Yang X-Q, Gu L, Liu X-S, Shi S-Q, Fu Z-W (2017) Antisite occupation induced single anionic redox chemistry and structural stabilization of layered sodium chromium sulfide. Nat Commun 8:566. https://doi.org/10.1038/s41467-017-00677-3
48. Wang T, Ren G-X, Shadike Z, Yue J-L, Cao M-H, Zhang J-N, Chen M-W, Yang X-Q, Bak S-M, Northrup P, Liu P, Liu X-S, Fu Z-W (2019) Anionic redox reaction in layered $NaCr_{2/3}Ti_{1/3}S_2$ through electron holes formation and dimerization of S-S. Nat Commun 10:1–12. https://doi.org/10.1038/s41467-019-12310-6
49. van Dinter J, Indris S, Bitter A, Grantz D, Cibin G, Etter M, Bensch W (2021) Long-term stable, high-capacity anode material for sodium-ion batteries: taking a closer look at $CrPS_4$ from an electrochemical and mechanistic point of view. ACS Appl Mater Interfaces 13:54936–54950. https://doi.org/10.1021/acsami.1c14980
50. van Dinter J, Grantz D, Bitter A, Bensch W (2022) A combined sodium intercalation and copper extrusion mechanism in the thiophosphate family: $CuCrP_2S_6$ as anode material in sodium-ion batteries. ChemElectroChem 9:e202200018. https://doi.org/10.1002/celc.202200018
51. Bongers PF, Van Bruggen CF, Koopstra J, Omloo WPFAM, Wiegers GA, Jellinek F (1968) Structures and magnetic properties of some metal (I) chromium (III) sulfides and selenides. J Phys Chem Solids 29:977–984. https://doi.org/10.1016/0022-3697(68)90234-5
52. Powell AV, Colgan DC, Ritter C (1997) A powder neutron diffraction study of structure and magnetism in $NiCr_2S_4$. J Solid State Chem 134:110–119. https://doi.org/10.1006/jssc.1997.7549
53. Morcrette M, Rozier P, Dupont L, Mugnier E, Sannier L, Galy J, Tarascon J-M (2003) A reversible copper extrusion–insertion electrode for rechargeable Li batteries. Nature Mater 2:755–761. https://doi.org/10.1038/nmat1002
54. Bodenez V, Dupont L, Morcrette M, Surcin C, Murphy DW, Tarascon J-M (2006) Copper extrusion/reinjection in Cu-based thiospinels by electrochemical and chemical routes. Chem Mater 18:4278–4287. https://doi.org/10.1021/cm060436z
55. Bensch W, Ophey J, Hain H, Gesswein H, Chen D, Mönig R, Gruber PA, Indris S (2012) Chemical and electrochemical insertion of Li into the spinel structure of $CuCr_2Se_4$: ex situ and in situ observations by X-ray diffraction and scanning electron microscopy. Phys Chem Chem Phys 14:7509. https://doi.org/10.1039/c2cp00064d
56. Tarascon J-M, Armand M (2001) Issues and challenges facing rechargeable lithium batteries. Nature 414:359–367. https://doi.org/10.1038/35104644
57. Goodenough JB, Kim Y (2010) Challenges for rechargeable Li batteries. Chem Mater 22:587–603. https://doi.org/10.1021/cm901452z
58. Whittingham MS (1976) Electrical energy storage and intercalation chemistry. Science 192:1126–1127. https://doi.org/10.1126/science.192.4244.1126
59. Yoshino A (2012) The Birth of the lithium-ion battery. Angew Chem Int Ed 51:5798–5800. https://doi.org/10.1002/anie.201105006
60. Morris BL, Plovnick RH, Wold A (1969) Magnetic susceptibility of some transition metal chalcogenides having the Cr_3S_4 structure. Solid State Commun 7:291–293. https://doi.org/10.1016/0038-1098(69)90402-5
61. Bouchard RJ, Wold A (1966) Structural and electrical properties of some monoclinic ternary sulfides*. J Phys Chem Solids 27:591–595. https://doi.org/10.1016/0022-3697(66)90203-4
62. Vaqueiro P, Hull S, Lebech B, Powell AV (1999) High temperature neutron diffraction studies of phase transformations in $NiCr_2S_4$. J Mater Chem 9:2859–2863. https://doi.org/10.1039/a904492b
63. Powell AV, Oestreich S (1996) Magnetic properties of ternary chromium sulfides, $V_xCr_{3-x}S_4$ ($0 \leqslant x \leqslant 1.0$). J Mater Chem 6:807–813. https://doi.org/10.1039/JM9960600807
64. Hayashi A, Ueda Y, Kosuge K, Murata H, Asano H, Watanabe N, Izumi F (1987) Cation distribution in (M′, $M_j)3S_e4$: I. (Cr, $T_i)3_S$e4. J Solid State Chem 67:346–353. https://doi.org/10.1016/0022-4596(87)90373-2
65. Lambert-Andron B, Berodias G, Chevreton M (1968) Étude par diffraction neutronique de $TiCr_2Se_4$ et $TiCr_2S_4$. Bull Minér 91:88–89. https://doi.org/10.3406/bulmi.1968.6191
66. Raccah PM, Bouchard RJ, Wold A (1966) Crystallographic study of chromium spinels. J Appl Phys 37:1436–1437. https://doi.org/10.1063/1.1708502
67. Afanasiev P, Thiollier A, Delichere P, Vrinat M (2000) Comprehension of the promoting effect in the MCr_2S_4 mixed sulfide catalysts. In: Corma A, Melo FV, Mendioroz S, Fierro JLG (eds) Studies in Surface Science and Catalysis. Elsevier, Granada, pp 473–478
68. Watanabe T (1973) Electrical properties of $FeCr_2S_4$ and $CoCr_2S_4$. Solid State Commun 12:355–358
69. Shirane G, Cox DE, Pickart SJ (1964) Magnetic structures in $FeCr_2S_4$ and $FeCr_2O_4$. J Appl Phys 35:954–955. https://doi.org/10.1063/1.1713556
70. Wold A, Dwight K (1993) Ternary transition metal chalcogenides AB_2X_4. In: Wold A, Dwight K (eds) Solid State Chemistry: Synthesis, Structure, and Properties of Selected Oxides and Sulfides. Springer, Netherlands, Dordrecht, pp 222–235
71. Momma K, Izumi F (2011) VESTA 3 for three-dimensional visualization of crystal, volumetric and morphology data. J Appl Crystallogr 44:1272–1276. https://doi.org/10.1107/S0021889811038970

72. Filik J, Ashton AW, Chang PCY, Chater PA, Day SJ, Drakopoulos M, Gerring MW, Hart ML, Magdysyuk OV, Michalik S, Smith A, Tang CC, Terrill NJ, Wharmby MT, Wilhelm H (2017) Processing two-dimensional X-ray diffraction and small-angle scattering data in DAWN 2. J Appl Crystallogr 50:959–966. https://doi.org/10.1107/S1600576717004708
73. Yang X, Juhas P, Farrow CL, Billinge SJL (2015) xPDFsuite: an end-to-end software solution for high throughput pair distribution function transformation, visualization and analysis. arXiv:1402.3163v3
74. Coelho AA (2016) Topas Academic (Version 6). Coelho Software, Brisbane, AU
75. Coelho AA (2018) TOPAS and TOPAS-Academic: an optimization program integrating computer algebra and crystallographic objects written in C++. J Appl Cryst 51:210–218. https://doi.org/10.1107/S1600576718000183
76. Balzar D, Audebrand N, Daymond MR, Fitch A, Hewat A, Langford JI, Le Bail A, Louër D, Masson O, McCowan CN, Popa NC, Stephens PW, Toby BH (2004) Size–strain line-broadening analysis of the ceria round-robin sample. J Appl Crystallogr 37:911–924. https://doi.org/10.1107/S0021889804022551
77. Coelho AA, Chater PA, Kern A (2015) Fast synthesis and refinement of the atomic pair distribution function. J Appl Crystallogr 48:869–875. https://doi.org/10.1107/S1600576715007487
78. Mangelsen S, Srinivasan BR, Schürmann U, Kienle L, Näther C, Bensch W (2019) Nanostructured tungsten sulfides: insights into precursor decomposition and the microstructure using X-ray scattering methods. Dalton Trans 48:1184–1201. https://doi.org/10.1039/C8DT04205E
79. Chevreton M, Sapet A (1965) Structure de V_3S_4 et de quelques sulfures ternaires isotypes. C R Acad Sci Paris 261:928–930
80. Watanabe T (1972) Growth of $CoCr_2S_4$ and $FeCr_2S_4$ single crystals by chemical vapor transport. J Phys Soc Jpn 32:1443–1443. https://doi.org/10.1143/JPSJ.32.1443
81. Shick LK, Von Neida AR (1969) Single crystal growth of $CoCr_2S_4$ and $FeCr_2S_4$. J Cryst Growth 5:313–314. https://doi.org/10.1016/0022-0248(69)90064-5
82. Goldstein L, Dormann J-L, Druilhe R, Guittard M, Gibart P (1973) Chemical transport of $FeCr_2S_4$. J Cryst Growth 20:24–28. https://doi.org/10.1016/0022-0248(73)90032-8
83. Riedel E, Al-Juani A, Rackwitz R, Söchtig H (1981) Spinelle mit substituierten Nichtmetallteilgittern. VIII. Röntgenographische und elektrische Eigenschaften, Mößbauer- und IR-Spektren des Systems $FeCr_2(S_{1-x}Se_x)_4$. Z anorg allg Chem 480:49–59. https://doi.org/10.1002/zaac.19814800906
84. Riedel E, Karl R (1981) Mössbauer studies of thiospinels. IV. The system $FeCr_2S_4$-Fe_3S_4. J Solid State Chem 38:48–54. https://doi.org/10.1016/0022-4596(81)90471-0
85. Hansen A-L, Kremer RK, Heppke EM, Lerch M, Bensch W (2021) Mechanochemical synthesis and magnetic characterization of nanosized cubic spinel $FeCr_2S_4$ particles. ACS Omega 6:13375–13383. https://doi.org/10.1021/acsomega.1c01412
86. Krengel M, Hansen A-L, Kaus M, Indris S, Wolff N, Kienle L, Westfal D, Bensch W (2017) CuV_2S_4: a high rate capacity and stable anode material for sodium ion batteries. ACS Appl Mater Interfaces 9:21283–21291. https://doi.org/10.1021/acsami.7b04739
87. Li J, Liu J, Sun Q, Banis MN, Sun X, Sham T-K (2017) Tracking the effect of sodium insertion/extraction in amorphous and anatase TiO_2 nanotubes. J Phys Chem C 121:11773–11782. https://doi.org/10.1021/acs.jpcc.7b01106
88. Tao H, Zhou M, Wang R, Wang K, Cheng S, Jiang K (2018) TiS_2 as an advanced conversion electrode for sodium-ion batteries with ultra-high capacity and long-cycle life. Advanced Science 5:1801021. https://doi.org/10.1002/advs.201801021
89. Vogt LO, El Kazzi M, Jämstorp Berg E, Pérez Villar S, Novák P, Villevieille C (2015) Understanding the interaction of the carbonates and binder in na-ion batteries: a combined bulk and surface study. Chem Mater 27:1210–1216. https://doi.org/10.1021/cm5039649
90. Song J, Xiao B, Lin Y, Xu K, Li X (2018) Interphases in sodium-ion batteries. Adv Energy Mater 8:1703082. https://doi.org/10.1002/aenm.201703082
91. Dahbi M, Nakano T, Yabuuchi N, Ishikawa T, Kubota K, Fukunishi M, Shibahara S, Son J-Y, Cui Y-T, Oji H, Komaba S (2014) Sodium carboxymethyl cellulose as a potential binder for hard-carbon negative electrodes in sodium-ion batteries. Electrochem Commun 44:66–69. https://doi.org/10.1016/j.elecom.2014.04.014
92. Crawford JA, Vest RW (1964) Electrical conductivity of single-crystal Cr_2O_3. J Appl Phys 35:2413–2418. https://doi.org/10.1063/1.1702871